

Detection, Characterization, and Localization of Interference Signals in Wideband GNSS Environments: the GIMAD System

Fran Fabra
IEEC-CERES
Universitat Autònoma de Barcelona
Barcelona, Spain
fabra@ieec.cat

Gonzalo Seco-Granados
IEEC-CERES
Universitat Autònoma de Barcelona
Barcelona, Spain
Gonzalo.Seco@uab.cat

José A. López-Salcedo
IEEC-CERES
Universitat Autònoma de Barcelona
Barcelona, Spain
Jose.Salcedo@uab.cat

Enric Obiols
Satellite Navigation Department
Indra Sistemas
Barcelona, Spain
eobiols@indra.es

Àngel Creus
Satellite Navigation Department
Indra Sistemas
Barcelona, Spain
acreus@indra.es

Antonio González-Novell
Satellite Navigation Department
Indra Sistemas
Barcelona, Spain
agnovell@indra.es

Abstract—We present in this paper a design for a monitoring station that will be part of a network of receivers in charge of providing a service for detection, characterization, and localization of interfering signals in safety critical GNSS environments. The purpose is to cover a wideband frequency range from 800 MHz to 1900 MHz with a power level mask taken from EGNOS and DFMC GBAS requirements. The proposed design combines two four-element arrays with two USRP units for collecting signals within the desired SNR margins. A comparative simulation study has been done to evaluate different techniques for interference detection, characterization, and estimation of its angle of arrival. The results show that a combination of power and kurtosis monitorization, both in temporal and frequency domains, is a proper solution to detect different types of interfering signals. In order to assure the best signal characterization, the use of the three selected techniques serves to overcome their respective limitations. For angle of arrival estimation, the fact of working in a suboptimal array configuration provides more robustness against outliers for certain geometries.

Index Terms—GNSS, Galileo, interference detection, jamming, localization

I. INTRODUCTION

Presence of interfering signals in the GNSS spectrum, located either in-band or in their vicinity, represent a thread for safety critical positioning, navigation, or timing (PNT) applications based on GNSS. In addition to the blind effect that a strong interference signal typically would cause to a standard GNSS receiver, also weaker signals, which could be unintentionally generated, need to be addressed in those environments. In this context, we are developing the GNSS Interference Monitoring and Detection (GIMAD) System in the frame of ESAs Navigation Innovation and Support Programme (NAVISP) to

efficiently detect and support the location of threads that could endanger satellite-based navigation activities. The equipment built is planned to work standalone or to be integrated into a network of several GIMAD units to widen the coverage area and enable interference localization. Moreover, the product supports the NAVISP objectives both from PNT user segment and from GNSS ground segment perspectives: support to law enforcement authorities, governmental users, agencies and operators in the monitoring of threats that can endanger the provision and usage of safety critical applications using satellite navigation and monitoring of the RF Environment in areas where GNSS ground infrastructure is deployed (e.g. EGNOS / Galileo reference stations or GBAS Ground Stations) and where the threats, in case they occur, may have a global impact on the provision of the system.

In this paper we present the design of the GIMAD unit. Section 2 provides the requirements of the system and an overview of the setup. Section 3 describes the state of the art for interference detection, characterization, and angle of arrival (AOA) estimation. The simulation study of the selected techniques and the results obtained are described in section 4. Finally, section 5 concludes the paper and gives some remarks for future work.

II. SYSTEM REQUIREMENTS AND SETUP DESCRIPTION

The GIMAD unit targets to monitor the whole frequency range from 800 MHz to 1900 MHz for detection, characterization, and AOA estimation of interfering signals. For the latter case, which seeks the localization of the interfering transmitter after combination of several GIMAD units, a requirement is set to achieve an accuracy of 60 degrees in azimuth for 95% of cases with a single interference source in GPS L1 and Galileo E1 . The threshold of minimum signal power to be detected is

set from a combination of several EGNOS and DFMC GBAS requirements and it is summarized in figure 1. The maximum input power level outside the GNSS bands is set to 0 dBW. In all the cases, these values are considered at the output port of a 0 dBi gain antenna. As it can be seen, the system has to deal with significant variations of power along the desired frequency band. For reference purposes, figure 1 also provides standard noise floor values and the maximum input power for a selected USRP unit (NI USRP-2945). We can see that while for some cases the input power must be reduced to protect the USRP unit, at the GNSS bands the received signal needs to be amplified by means of an LNA at the beginning of the RF chain to keep enough SNR.

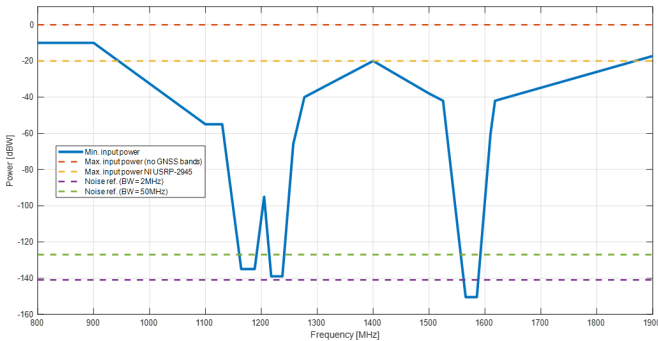


Fig. 1. Power level threshold for interference signal detection (solid line).

In order to fulfil the previous requirements, a whole setup (GIMAD unit) has been designed which is essentially composed by three main blocks: antenna front-end, reception set and computer unit. The first block includes the antenna (single or array) and the different RF components required to deliver the collected analog signal to the inputs of the next block inside the proper power level margins: amplifiers, power splitters, bias-tee, coaxial cables, etc. The second block is responsible of digitize, filter and down-convert the analog signal into base-band digital IQ samples. For such purpose, two USRP instruments are employed with a GNSS disciplined reference clock to synchronize them. In addition, a GNSS receiver is employed to deliver GNSS observables and internal information. Finally, a computer unit is in charge of the storage and processing of the datasets delivered by the previous block.

Figure 2 shows a scheme of the elements that conform the two first blocks. The design of the setup aims to fulfil the next purposes:

- GNSS monitoring: The upper branch in the scheme from figure 2 allows to analyze GNSS observables acquired through a GNSS receiver.
- In-band monitoring: Two of the outputs from the power splitter connected to the single GNSS antenna provide two channels to USRP-1 for monitoring raw data at the GNSS bands around GPS L1 and L5 frequencies (covering both GPS and Galileo).
- Out-of-band monitoring: The remaining bands covering the 800-1900 MHz frequency range shall be also moni-

tored. Such wideband range includes both high and low (e.g., GPS L2) input power requirements. To achieve this, the remaining output from the power splitter provides a channel for properly monitoring the sub-band around GPS L2 frequency. A single wideband antenna is connected to an attenuator to provide an additional channel to USRP-1 for monitoring other sub-band with higher power levels. The rest of sub-bands are acquired through the array system connected to USRP-2 in a random sequential strategy.

- Angle-of-arrival estimation: The capability to apply localization methods by acquiring signals from 4 synchronized channels at any sub-band within 800-1900 MHz is achieved by means of the array system connected to USRP-2. Given that these elements are also employed for the out-of-band scanning by default, the idea is to only run the localization mode (the four channels acquire data at the same frequency band) whenever the real-time interference detection routines trigger an alarm at a given band. The combination of two four-element arrays allows to compensate the important differences of input power along the wideband range to keep both proper SNR values and safe power levels at the input of the USRP units in all the cases. The elements of each array are distributed to form a square shape with to $\lambda_{L1}/2$ of side length (GPS L1 as a reference frequency).

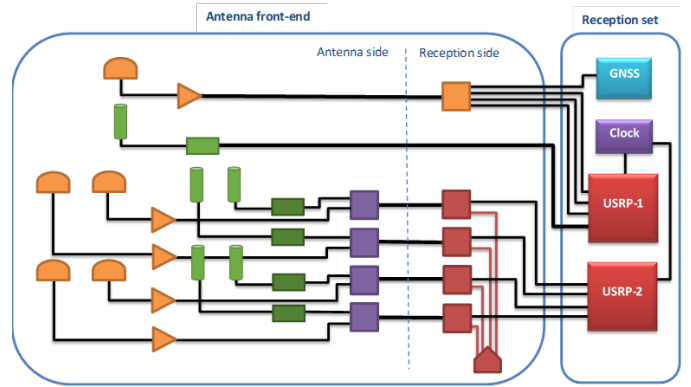


Fig. 2. Scheme of antenna front-end and reception set of the GIMAD unit. The description of the different elements from the antenna front-end is given in figure 3.

III. STATE OF THE ART INTERFERENCE DETECTION, CHARACTERIZATION, AND LOCALIZATION TECHNIQUES

Due to the historical importance of navigation and the increasing use of GNSS-based applications nowadays, there is a vast literature addressing the impact of interfering signals and their mitigation in this field. Two particular aspects of GNSS make this task more challenging compared against other RF technologies: (1) by being designed to lie below the noise level, GNSS signals are weak, so just a small power source can cause problems; and (2), as a long-term satellite-based system

SYMBOL	DESCRIPTION
	GNSS antenna (GPS L1/L2/L5 and Galileo E1/E5a)
	LNA for GNSS band (GPS L1/L2/L5 and Galileo E1/E5a)
	Power splitter with 1 input port and 4 output ports
	Wideband antenna (800-1900 MHz)
	Attenuator for wideband frequency range (800-1900 MHz)
	Attenuator for wideband frequency range (800-1900 MHz) with DC-block
	Power combiner with 2 input ports and 1 output port
	Bias-tee
	DC power supply (5-12 V)

Fig. 3. Description of the different elements of the antenna front-end given in scheme from figure 2.

broadcasting signals all over the Earth surface, no adaptability to interference events can be expected from the transmitter side.

A first step consists in the detection of the interference itself. As described in section 3.1, this can be simply achieved by monitoring a set of variables from the GNSS receiver, whose selection generally depends on the interference scenario. However, given that the nature of the interference is to cause a clear degradation, its detection does not represent a difficult issue and thus the research on this aspect is rather limited. On the other hand, interference mitigation is a more demanding aspect and several studies have addressed it from different perspectives during the last years, but this aspect is not envisaged for the GIMAD unit. However, there is not an optimal solution valid for all type of scenarios, and the use of any technique has associated a set of trade-offs. For this reason, it is also important to properly characterize the interfering signal and some methodologies to achieve this objective are described in section 3.2.

Finally, localization of interference transmitters is a key aspect for their effective clearance or impacts minimization. However, a combination of more than one receiver is generally required to achieve this purpose (at least 3 for static stations) under certain geometrical conditions. There are three main possibilities to estimate the localization of the transmitter based on different observables: (1) the time difference of arrival (TDOA) of a signal reaching each pair of receivers [1] [2], (2) the power decay suffered by the signal properly calibrated for being proportional to the travelled distance (e.g., [1]), and (3) the angle of arrival estimations as seen from the different receivers. From the point of view from a single GIMAD unit, the two first options only require time and power measurements. However, the estimation of the angle of arrival is not straightforward and section 3.3 provides methods to properly address it.

A. Interference detection

Interfering signals clearly degrade the behavior of standard GNSS receivers. Therefore, their detection can be achieved simply by monitoring some variables on the reception chain. Some examples can be found in (e.g., [2], [3], [4]). We can classify these variables into two main categories depending on which part of the GNSS receiver architecture are taken: prior or after the PRN cross-correlation process (something like level-1 and level-2 observables). The first group then allows a quicker detection, while the second group provides additional information about the impact on the receiver.

1) *Pre-correlation techniques*: In the first category, the raw data complex samples collected by the receiver are analyzed. Two main aspects are checked: statistics and power. In the first case, it is exploited the fact that an interference-free signal in the GNSS bands should be a zero-mean Gaussian stochastic process. Then, a normality test can be applied for evaluating the detection of interfering signals with non-Gaussian properties, such as a goodness of fit measurement of the histogram or autocorrelation of data snapshots. In [5], ten well-known different techniques are analyzed under typical interference models in a radiometry scenario, which is equivalent to GNSS in this context, showing that the best performance is obtained by simply evaluating the kurtosis of the data snapshots. The only limitation of this approach is that it has a blind spot for interfering signals with a 50% duty cycle. For this reason, it is recommended to be complemented with an additional normality test not blind at these situations. The previous analysis [5] suggests the Anderson-Darling test for this task. Another possibility, not included in [5], is to evaluate the normalized sixth cumulant [6], which is given by k_6/μ_2^3 , where:

$$k_6 = \mu_6 - 15\mu_4\mu_2 - 10\mu_3^2 + 30\mu_2^3 \quad (1)$$

and μ_n is the n th central moment. As a comparison, the kurtosis is given by μ_4/σ^4 . This metric can cover the aforementioned blind-spot of the kurtosis. The second aspect to be checked with raw samples is the power level. As already mentioned, this level corresponds to the background noise in a GNSS band under an interference-free scenario. Therefore, clear power variations from such reference level are indicators of interference presence. The methodology to follow is simply to monitor the time evolution of power estimates from data snapshots comparing them against a given threshold. This can be also done in an indirect way from the gain values of the GNSS receiver provided by the automatic gain control (AGC) unit. In addition, the power level can be checked in the frequency domain by means of FFT of data snapshots. Moreover, both time and frequency domains can be simultaneously scanned using the same techniques for interference characterization described in next section 3.2, as done in (e.g., [7], [8]).

Finally, it is worth mentioning that there are further pre-correlation techniques, such as to monitor the variables from an adaptive notch filter applied to the data snapshots (e.g.,

[9], [10]) or to check the singular value decomposition of their covariance matrix [11]. Both methods show a good performance for detecting continuous wave tones but fail for pulsed and chirp signals respectively.

2) *Post-correlation techniques*: The second category of variables accounts for those obtained after cross-correlation inside the GNSS receiver, such as C/N0 values, pseudo-range and carrier phase deviation and position accuracy among other parameters. Interfering signals have an impact on them, which can be monitored by comparing the expected time evolution of each parameter against certain thresholds to determine the impact of an interference in the receiver in terms of accuracy, integrity and continuity. Since the variables can be affected by a wide variety of factors different from interference e.g., multipath or elevation of the transmitter satellite, thresholds should be computed accounting for these effects [2] [12].

Another possibility is to analyze variations in the cross-correlation curve [13], which is usually referred as signal quality monitoring (SQM). The basis of this type of approach is to check the statistical consistency between the nominal correlation function and the cross-correlation samples, which would be corrupted under the presence of interfering signals. An important limitation of this kind of method is the difficulty for discriminating between interference-induced effects and natural multipath.

B. Interference characterization

Interfering signals can be generated by different type of sources, both accidental, such as radiated harmonics from electronic instrumentation or signal leakage from a bad designed RF system at a neighbor frequency band, or intentional, such as jamming devices. Therefore, there is a wide variety of interfering signals that can degrade the behavior of a GNSS receiver.

Typically, we can classify RFI signals from its power distribution in time and frequency domains. Figure 4 illustrates this concept by showing the most common interfering signals: single and multi-tone, wide-band noise, frequency modulated (chirp) and a combination of them, with continuous or pulsed transmission. Given that the performance of the mitigation technique varies among the different cases, this type of characterization benefits the proper selection of the required counter-measurements.

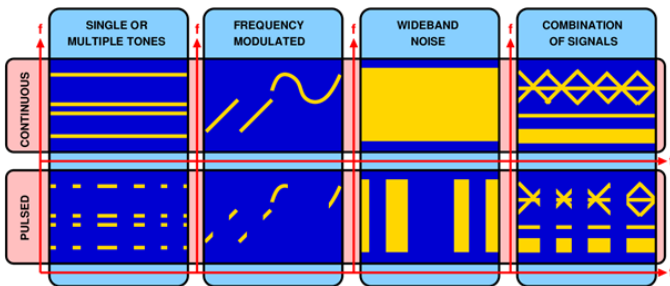


Fig. 4. Classification of interfering signals according to their time-frequency power distribution.

Time-frequency representation belongs to the field of spectral estimation in signal processing. The most common technique is the spectrogram, whose discrete time expression is defined as

$$S(n, f) = |\text{STFT}(n, f)|^2 \quad (2)$$

where STFT is the short-time Fourier transform of the input signal $s[n]$

$$\text{STFT}(n, f) = \sum_{i=n}^{n+L-1} s[i]w[i-n]e^{-j2\pi if} \quad (3)$$

and $w[n]$ is the analysis window of length L . This value determines the tradeoff between temporal and frequency resolution. Moreover, the type of window defines an additional tradeoff between width of the main lobe (spectral resolution) and beam-ratio with respect to side-lobes (spectral leakage), being Hann and Hamming windows common choices. In spite of its limitations, the spectrogram has a relatively low computational cost (availability of efficient Fourier transform implementations) and it is suitable for real-time applications.

In order to overcome the time versus frequency resolution tradeoff problem, another possibility of representation is the Wigner-ville distribution, whose discrete time implementation is given by [3]:

$$\text{WVD}(n, f) = \sum_i s[n+i]s^*[n-i]e^{-j4\pi if} \quad (4)$$

where $s[n]$ is the input signal. In practice, a finite interval of $s[n]$ is available, so the previous equation is actually multiplied by a window function (the summation has lower and upper limits). Compared against the spectrogram, the price paid to achieve high resolution in both domains is a higher computational cost and the possible presence of cross-terms in the results.

Finally, an additional means for interference characterization is based on analysis of cyclostationary properties of the received signal. In general, while most communication signals show temporal variability on their statistics (they are non-stationary), they still exhibit periodic behavior (cyclostationarity). In this context, the autocorrelation function of a cyclostationary signal $x[t]$ can be represented by a Fourier series

$$R_x(t, \tau) = \sum_{\alpha} R_x^{\alpha}(\tau)e^{-j2\pi\alpha t} \quad (5)$$

where R_x^{α} is called the cyclic autocorrelation function (CAF) of cycle frequency and can be computed as

$$R_x^{\alpha}(\tau) = \lim_{T \rightarrow \infty} \frac{1}{T} \int_{-T/2}^{T/2} x(t+\tau/2)x^*(t-\tau/2)e^{-j2\pi\alpha t} dt \quad (6)$$

Its conjugate version is obtained after removing the conjugation of the second term inside the integration. Then, we can compute the cyclic spectral correlation or cyclostationary spectrum as the Fourier transform of the CAF by following the Wiener-Khinchin theorem. The relevant aspect of this analysis comes out by the fact that this type of spectral representation

enables the separability among signals with different modulation which would be overlapped in the standard power spectral density, as illustrated in Figure 5. Effective estimators for the cyclic spectral correlation can be found in [14].

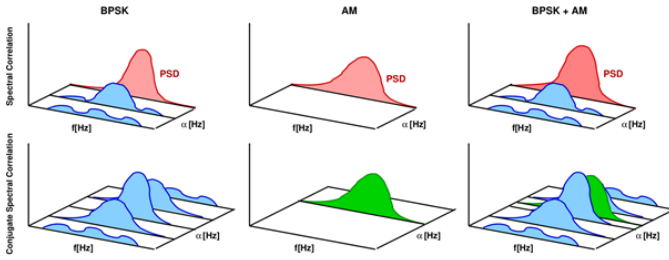


Fig. 5. Representation of cyclic spectral correlation (upper plots) and its conjugate (bottom plots) for different signals with periodic statistics based on the modulation of their components. From left to right: BPSK, AM and a combination of both. The last case illustrates the capability of this kind of representation for separating both modulation components, while the power spectral density (contained in the spectral correlation for $\alpha = 0$) mixes them up.

C. Estimation of angle of arrival

The main requirement to estimate the AOA or direction of arrival (DOA) from a single receiver is to coherently combine the inputs from several antennae, or antenna array. If we include the narrow-band condition (delay increments can be approximated by phase rotations), which holds for the GNSS case (bandwidth is rather smaller than carrier frequency), then AOA estimation is equivalent to spectral estimation [15]. In this context, there are several standard approaches ranging between three well-known techniques (summarized in table I):

- **Beamformer:** equivalent to a periodogram, it is the simplest approach. Basically, it consists in scanning over the product of the beamforming vector and the spatial correlation matrix of the array samples in order to find the maximum values, which are directly related to the AOA of the incoming signals. Its main limitation is that the angle resolution is directly proportional to the number of array elements, which in general is rather low for a standard setup.
- **Capon:** developed from the minimization problem of the output power for spatial filter design, the method consists in scanning over the inverse of the product of the beamforming vector and the inverse of the spatial correlation matrix of the array samples to obtain the location of the largest peaks, which are the AOA estimates. Despite achieving better results than the beamformer, its angular resolution is still rather limited.
- **MUSIC:** standing for Multiple Signal Classification, it is a more complex approach that achieves the best angle resolution. It requires the singular value decomposition of the spatial correlation matrix of the array samples, which can be computationally demanding for a large number of antenna elements. The singular values obtained are related to the power levels of the incoming signals and the background noise, which is contained in all of

them. Then, the singular vectors associated to the smaller singular values define the space without signal contribution (only noise). By combination with the beamforming vector it can be built an equation whose solution provides the estimation of the AOA of the incoming signals. The main limitation of this technique is that the number of array elements N determines the maximum number of simultaneous interfering signals to $N - 1$.

TABLE I
BASIC PROCEDURES FOR AOA ESTIMATION FROM THE SPATIAL CORRELATION MATRIX R

Algorithm:	Beamformer	Capon	MUSIC
Define steering vector a as a function of AOA θ and then scan over:	$a^H(\theta)Ra(\theta)$	$\frac{1}{a^H(\theta)R^{-1}a(\theta)}$	$\frac{1}{a^H(\theta)UU^H a(\theta)}$

The term U in MUSIC is obtained from singular value decomposition of R .

By reviewing the last research studies on spectral AOA estimation, we can see that most of them are based on solving practical issues of the MUSIC approach, such as the extension to a broadband case [16] [17] or the reduction of the computational complexity for large arrays [18], which are not required for the present study case. Other AOA techniques that have been also discarded are parametric subspace-based methods like ESPRIT [19], which require linearly distributed arrays, or deterministic parametric estimation methods such as the Expectation Maximization (EM) algorithm [20] and the Space Alternating Expectation Maximization (SAGE) [21] due to their increased computational complexity.

IV. SIMULATION ANALYSIS

A. Detection analysis

From the interference detection techniques reviewed in section 3.1, we will focus here on the pre-correlation ones because they are not subjected to any particular characteristic of the visibility scenario in a GNSS environment. In addition to the monitorization of the received power level, which is the reference methodology for detection of unexpected signals in a known frequency band, we also select the monitorization of the kurtosis due to the benefits in terms of calibration requirements of the statistical methods (a normal distribution is assumed by default). However, given that this technique has a blind spot for signals with 50% of duty cycle, we also include two alternatives (also in the category of statistical methods) for covering this case: Anderson-Darling test and monitorization of the 6th order cumulant.

A set of Monte-Carlo runs has been done to assess the detection capability of the selected techniques under different scenarios. In particular, four type of continuous wave interference signals and five different interference-to-noise ratio (INR) levels are selected. The detection algorithms are tested under all resultant combinations. The number of simulation runs is set to 10^5 and the length of the snapshot is 1024 samples. The

procedure simply consists in fixing a probability of false alarm ($p_{fa} = 0.05$) value to obtain a threshold level from the algorithm's metric by applying a series of noise sequences (absence of interference signal). Then, the corresponding probability of detection (pd) value is obtained by injecting the interference signal into the simulations and setting the previous threshold in the detection algorithm. It is important to remark that the detection techniques are evaluated both against the standard time-based snapshot of the interference signal model and its frequency-based version obtained by means of FFT.

Before checking the results obtained, it is worth mentioning that only the biggest INR value (3 dB) represents a situation where the interference power level is above the noise floor. In the other cases, the signal to be detected is either comparable (0 and -5 dB) or clearly under the background noise (-10 and -20 dB), being the latter a particularly challenging scenario. The purpose of including such small power values here is to reach the limits of detection capability from the different techniques. Recall from figure 1 that the minimum INR value expected in this project is higher than -10 dB, being most of the cases well above the noise level.

Figure 6 shows the results obtained from the simulation analysis. We can see that the power level algorithm achieves high performance in all cases, but it is a method that requires full and dedicated calibration for each receiver (GIMAD unit). On the other hand, algorithms based on normalization tests achieve a more limited performance under less restrictive calibration requirements. It is relevant to see how the application of the FFT to the snapshots has a strong impact on these techniques. As expected, algorithms based on normalization tests do not work for noise-like signals with gaussian distribution. Despite the results, the combination of both power and normalization methods is still useful given that the second ones might be employed to adapt the threshold levels of the former by performing a first estimation of the noise floor level.

In order to further compare the different normalization algorithms evaluated, the same exercises have been done for interfering signals with 50% of duty cycle, which is a known blind spot for the monitorization of the kurtosis. The results are shown in figure 7. The two alternatives (6th order cumulant and Anderson-Darling test) show a rather limited performance for the INR values evaluated. Again, a significant improvement is obtained when using frequency-based snapshots for the given interfering signal models, even for the kurtosis. Therefore, the use of the latter technique, both in time and frequency domains seems to be a sufficient means to combine with the monitorization of the power level for interference detection in all the scenario cases under test.

B. Comparison of characterization methods

The characterization methods described in section 3.2 provide means to identify the behavior of signals in both temporal and frequency domains (spectrogram and Wigner-Ville distribution) or to check cyclostationary aspects that typically characterize certain type of communication signals. Figures 8 and 9 provide two selected simulation cases that try to illus-

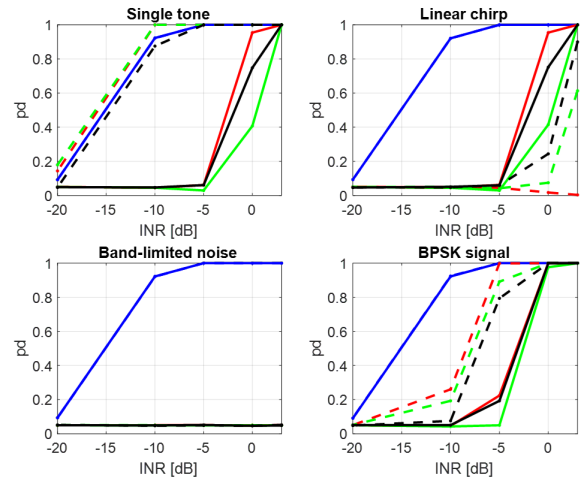


Fig. 6. Probability of detection results as a function of INR for a $p_{fa}=0.05$. Each panel provides the results for a type of interfering signal. A color-code indicates the methodology evaluated: power level monitorization (blue), kurtosis monitorization (red), 6th order cumulant (green), and Anderson-Darling test (black). Solid lines are used for time-based snapshots while dashed lines indicate frequency-based snapshots.

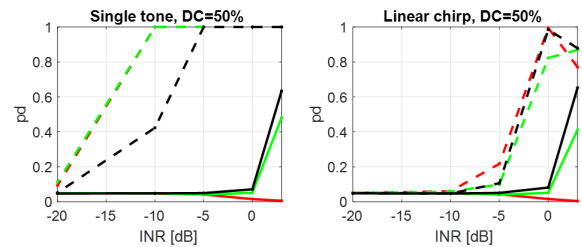


Fig. 7. Probability of detection results for normalization methods as a function of INR for a $p_{fa}=0.05$. Each panel provides the results for a type of interfering signal with a duty cycle of 50%. A color-code indicates the methodology evaluated: kurtosis monitorization (red), 6th order cumulant (green), and Anderson-Darling test (black). Solid lines are used for time-based snapshots while dashed lines indicate frequency-based snapshots.

trate the most relevant properties of those methodologies. On the first case a linear chirp signal interfering signal is properly characterized by the spectrogram with limited resolution. On the other hand, the Wigner-Ville distribution achieves very high resolution, but the price paid is the appearance of artifacts in the results (the real components are those that coincide with their equivalent location at the corresponding spectrogram). The cyclostationary spectrum provides the power spectral density at the cut with $\alpha = 0$, which is blurred by the displacement of the tone in the frequency domain for the observation interval (as shown by the former techniques). The values for $\alpha > 0$ do not provide relevant information. The second case, illustrated in figure 9, is a BPSK interfering signal. While neither the spectrogram nor the Wigner-Ville distribution provides further information than a power increase region bounded to certain frequency interval, the cyclostationary spectrum shows a unique pattern in the cyclic frequential domain (α) which is characteristic for this type

of modulation. Overall, the combination of the three methods covers their single limitations for characterization purposes.

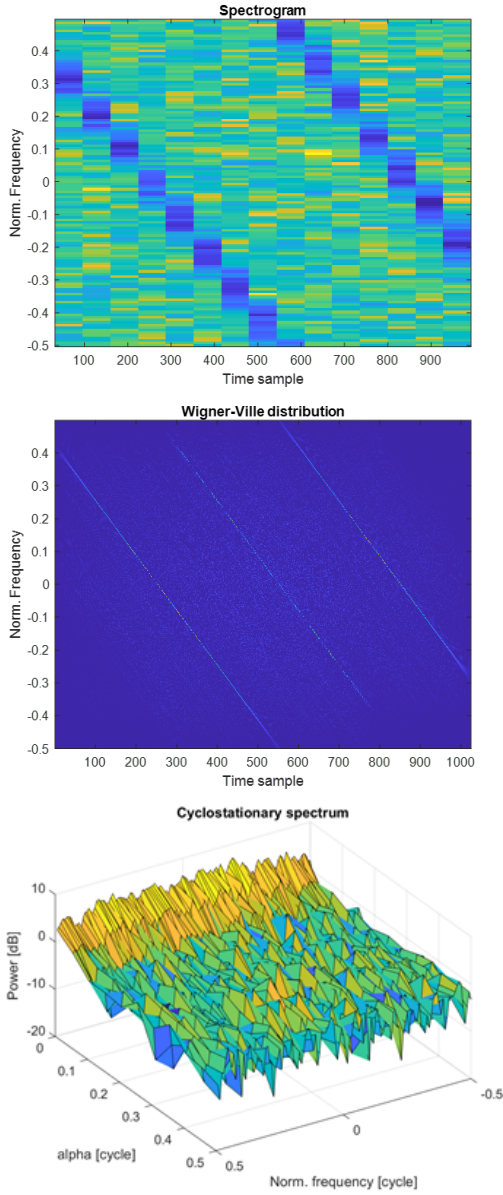


Fig. 8. Example of characterization methods applied to a linear chirp interfering signal with INR=3dB.

C. Analysis of angle of arrival estimation

Simulation runs have been also done to evaluate the performance of localization algorithms. Three degrees of freedom define the different scenarios evaluated: interference to noise ratio (INR), number of simultaneous interference signals and frequency band. The first parameter shows the degradation caused by a reduction of the signal power. Values of 3, 0, -5 and -10 dB are taken. The number of interference signals, ranging from 1 to 4, provide information on the capability of the different methods to obtain valid solutions in scenarios with multiple signals due to their intrinsic angle resolution.

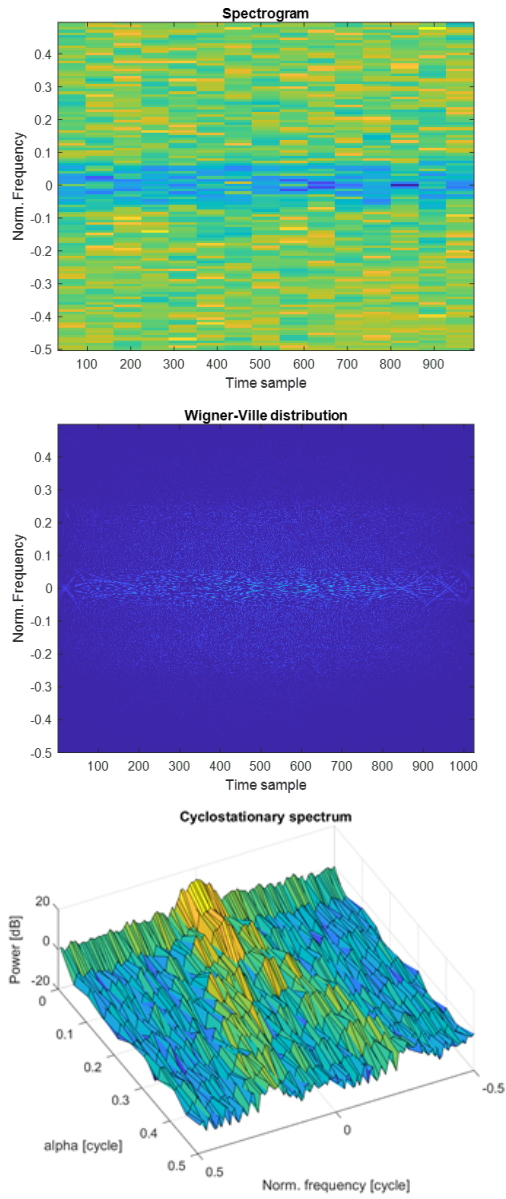


Fig. 9. Example of characterization methods applied to a BPSK interfering signal with INR=3dB.

The type of signals is randomly selected in each run among the same options employed during the detection analysis. Finally, by taking into account that the physical separation of the four elements in the arrays is set to $\lambda_{L1}/2$ (each side of the square shape), four frequencies (carrier frequency of the interference signal) are evaluated to check the impact of variation in angle resolution and addition of ambiguity ranges: GPS L1, GPS L5, 800 MHz and 1900 MHz. The number of simulations for each scenario is set to 10^5 .

Before entering the results, it is worth looking the general behavior of the different algorithms for the same input. As indicated in table I, the procedure is to define a steering vector as a function of the shape of the array and the AOA (or

azimuth) and then to scan the corresponding equation. The result is a function of the AOA known as spatial spectrum, whose peaks provide the AOA estimations of the interference signals. Figure 10 illustrates the differences between the results obtained with the techniques under analysis. As we can see, all of them properly estimate the AOA (indicated with a vertical line) regardless the width of the corresponding peak. However, beamformer and Capon show additional lobes that could induce fake estimations events in this case. Regarding the impact of INR reduction, we can see that the dynamic range is reduced but the main peak still properly estimates the AOA. The results obtained when increasing the number of interference signals are illustrated in figure 11, where it stands out the importance of having good angular resolution for getting more accurate AOA estimations.

The fact of having secondary lobes in the spatial spectrum imposes the requirement to include a methodology to determine the actual number of interference signals (it would be wrong to assign an AOA estimation to each peak). The methodology selected is the minimum description length (MDL), which establishes a decision criterion based on the singular values from the spatial correlation matrix.

The results obtained in the analysis based on GPS L1 carrier frequency, which also apply for Galileo E1, are given in figure 12, which provides the probabilities of detection (pd) and the percentile for 30° of AOA error in absolute value, which corresponds to an AOA error beam of 60° (our reference requirement for a single interfering signal in GPS L1 band). It is important to remark here that, in this context, the probability of detection concept is related to the capability of the procedure to obtain an AOA estimation for each of the interfering signals injected, not to the detection of the signals themselves. From the evolution of both variables as a function of #s obtained in the results, we can see that the algorithms with lower angular resolution loss more cases and show larger errors in AOA estimation when increasing #s (less peaks available). Even the case with #s=4, which is above the limit for MUSIC, does not show a clear degradation of this method with respect to the others (the relatively small the number of elements in the array sets a performance limit regardless the technique employed). As expected, all of them have a degradation of the performance when decreasing INR.

A relevant aspect is to see that even for a single interfering signal (#s = 1), all the methods have some percentage of AOA estimations with relatively large errors. In order to know if there is a systematic effect behind this issue, we can check the AOA error distribution as a function of the AOA (or azimuth). Figure 13 provides these results for different values of INR and a single interference signal. We can see that, while most values are concentrated around zero error, there are outliers around AOA values of 0°, 90°, 180° and 270° (with a spreading of the concentration areas as INR decreases). These values correspond to the directions that are perpendicular to the sides of the square-shaped array. The lowest spatial diversity in the array happens at these geometries because the phase values of two couples of elements coincide. In addition, due to the

$\lambda_{L1}/2$ separation of elements, there can be ambiguity between the original AOA value and its opposite direction (this is why the error goes up to 180°).

At GPS L5, the carrier wavelength is longer than twice the physical distance of the sides of the array, which would be the optimal one, thus producing a reduction of the angular resolution achievable by the array (regardless the localization technique). This effect can be imagined as a spreading of the beams in the spatial spectrum from figures 10 and 11. The results from figure 14 show a decrease of pd with respect to GPS L1 wavelength, which is directly related to the previous effect. However, the general loss of angular resolution eliminates the appearance of outliers with 180° of error for a single interfering signal. The percentile results reveal that such effect produces a general improvement with respect to the results obtained in L1. Therefore, having the array working in suboptimal conditions clearly benefits the AOA estimation.

The next carrier frequency under analysis is 800 MHz, which is the lowest value of the frequency range that aims to be covered by the GIMAD unit. Figure 15 provide the results obtained with that configuration. Essentially, by using a lower frequency, the results obtained represent a step forward on the effects seen in L5: there is a clear degradation in both metrics due to the further reduction on angular resolution, although it still compensates the impact produced by presence of outliers in L1.

Finally, the last frequency analyzed is 1900 MHz, which is located at the other end of the desired frequency range. The novelty in this case is that the wavelength is shorter than the optimal value from the physical dimensions of the array, thus increasing the angle resolution at the price of adding a range of ambiguity values (AOA's with more than one solution). Figure 16 provide the results obtained in this case. Both probability metrics increase a bit with respect to L1 due to such improvement on angular resolution. However, in terms of AOA error, the results for a single interference signal are better than in L1 because the outliers are not concentrated around 180° of error. Despite this, by checking the results of the percentiles, we can see that the general behavior is quite similar to the L1 case.

From the results obtained, to remove outliers at the price of losing angular resolution is proved to be a proper solution. We can achieve this effect simply by reducing the physical separation between array elements. Therefore, a modification in the GNSS array is made: to reduce the side of the square shape from $\lambda_{L1}/2$ to $\lambda_{L1}/3$. The reduction cannot be applied to the wideband array due to the physical dimensions of the single antenna element selected (it is kept to $\lambda_{L1}/2$).

The simulations have been repeated under the proposed array modification for carrier frequencies GPS L1 and GPS L5. The results obtained are given in figures 17 and 18. From the AOA error values with a single interference signal, we clearly see that the outliers have been removed from the L1 case. The results from the percentiles show a general improvement in all the scenarios. The L5 case shows a minor degradation due to the additional decrease of the angular resolution, although is

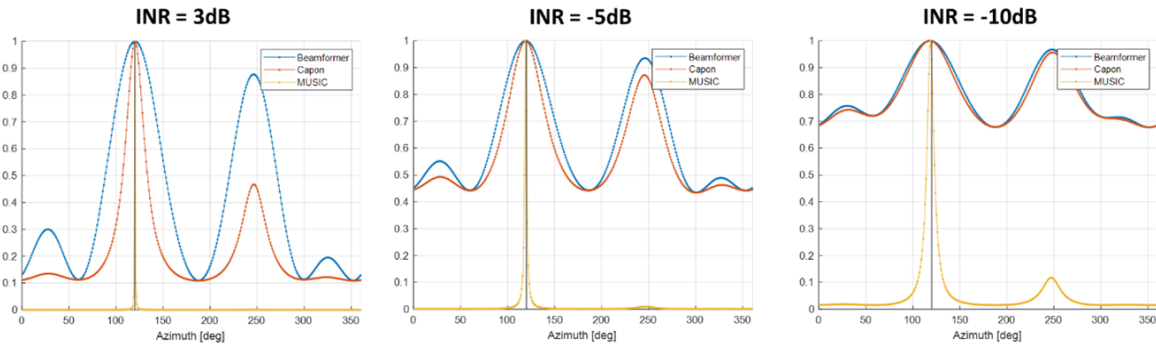


Fig. 10. Example of impact of INR variation in spatial spectrum for the different localization techniques for a single interference signal case. The actual AOA value is marked with a vertical line.

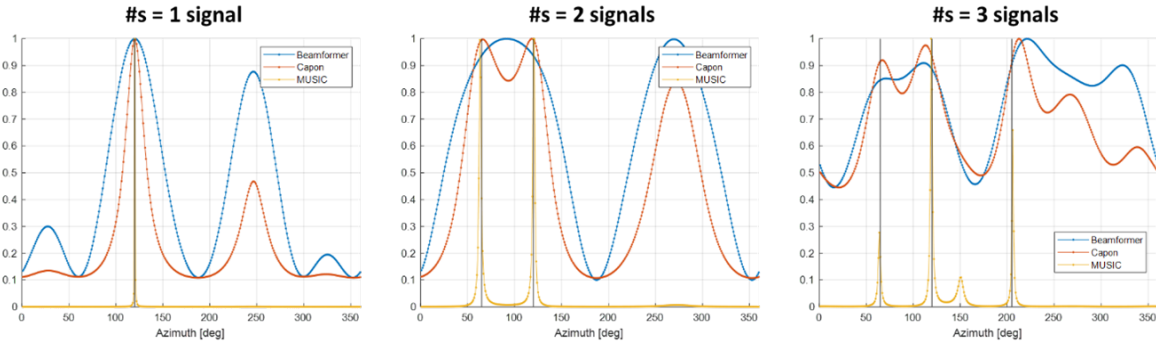


Fig. 11. Example of impact of increase of interference signals in spatial spectrum for the different localization techniques. The actual AOA values are marked with vertical lines.

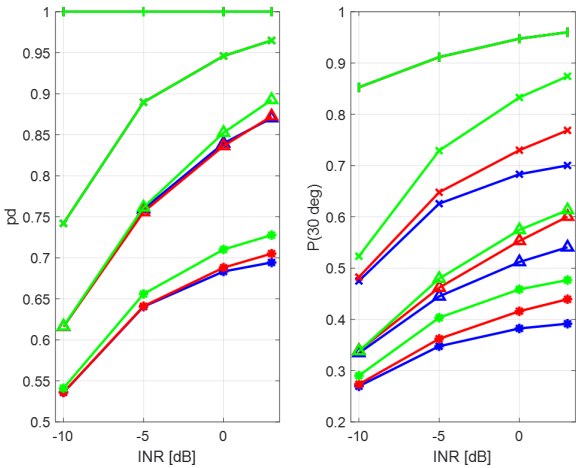


Fig. 12. [Left side] Probability of detection (AOA context) for the different techniques and number of interfering signals ($\#s$) as a function of INR. [Right side] Percentile 30° of AOA error in absolute value for the different techniques and number of interfering signals ($\#s$) as a function of INR. The frequency evaluated is GPS L1 and the side of the square-shape array is $\lambda_{L1}/2$. The color indicates the AOA estimation technique evaluated: beamformer in blue, Capon in red and MUSIC in green. The marker indicates the number of interfering signals injected in the simulation: | for $\#s = 1$, \times for $\#s = 2$, \triangle for $\#s = 3$ and $*$ for $\#s = 4$ (the number of straight lines required to make the symbol is equal to $\#s$).

a price worth paid for the outlier removal in L1.

V. CONCLUDING REMARKS AND FUTURE WORK

The GIMAD framework has been presented. With the purpose of designing a network of monitorization of interfering signals in GNSS environments, a station unit has been designed capable to monitor a wideband frequency range (800-1900 MHz) to trigger an alarm event when an interfering signal is present and to perform an AOA estimation for later localization of its transmitter. Based on EGNOS and DFMC GBAS requirements, a power level mask with a high dynamic range along the frequency range is selected, which imposes to address both high and low power inputs to avoid damaging the USRP unit and to achieve enough SNR values.

Different simulation studies have been done to check the performance of the different algorithms selected for each of the targets of the project. For interference detection, whose analysis has been limited to the pre-correlation methods, the results show that the combination of the monitorization of power level and kurtosis, both in time and frequency snapshots, provides a good means to cover all the scenarios under analysis, where the second variable might enable an adaptative calibration of the noise floor level. Regarding characterization, the use of the three methodologies (spectrogram, Wigner-Ville distribution and cyclostationary spectrum) properly captures all the details that might be employed for identifying the

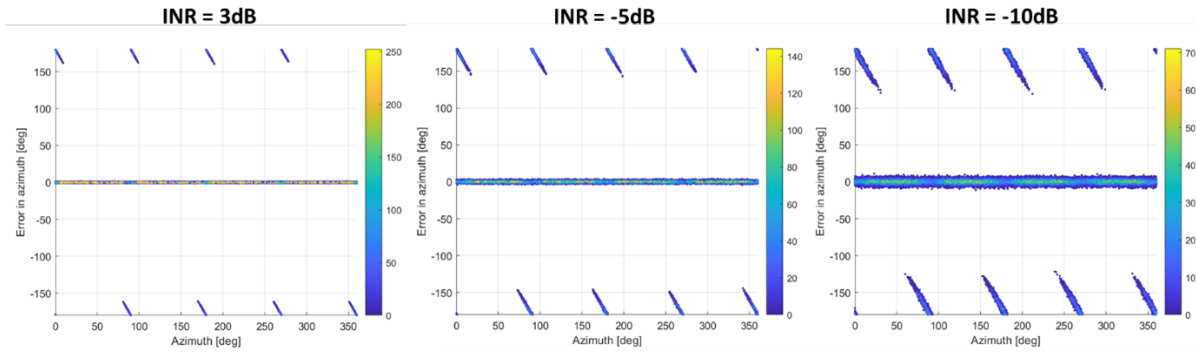


Fig. 13. Distribution of error in AOA for the corresponding value of AOA (or azimuth). Different values of INR are set on the different panels. A single interference signal is considered using MUSIC (the other algorithms show the same type of behavior). The color indicates the number of points in the area (density plot), as indicated in the vertical bar. The carrier frequency of the signals is set to GPS L1 and the length of the side of the four-element square-shaped array is set to $\lambda_{L1}/2$.

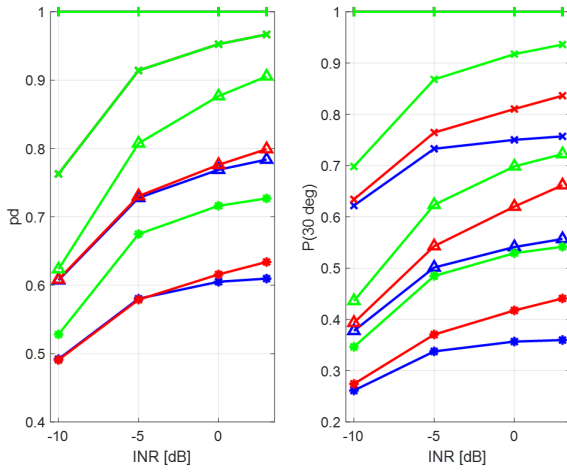


Fig. 14. [Left side] Probability of detection (AOA context) for the different techniques and number of interfering signals ($\#s$) as a function of INR. [Right side] Percentile 30° of AOA error in absolute value for the different techniques and number of interfering signals ($\#s$) as a function of INR. The frequency evaluated is GPS L5 and the side of the square-shape array is $\lambda_{L1}/2$. The color indicates the AOA estimation technique evaluated: beamformer in blue, Capon in red and MUSIC in green. The marker indicates the number of interfering signals injected in the simulation: | for $\#s = 1$, \times for $\#s = 2$, Δ for $\#s = 3$ and $*$ for $\#s = 4$ (the number of straight lines required to make the symbol is equal to $\#s$).

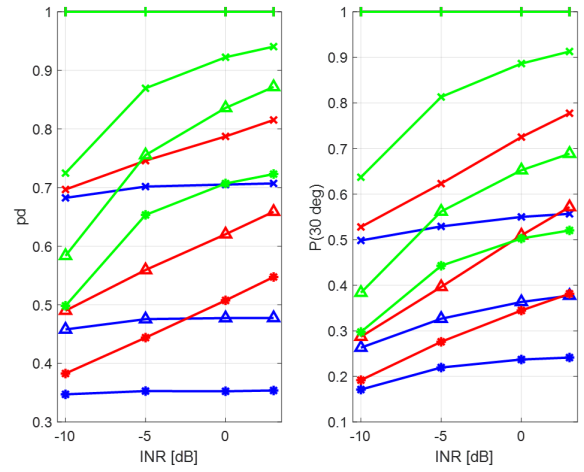


Fig. 15. [Left side] Probability of detection (AOA context) for the different techniques and number of interfering signals ($\#s$) as a function of INR. [Right side] Percentile 30° of AOA error in absolute value for the different techniques and number of interfering signals ($\#s$) as a function of INR. The frequency evaluated is 800 MHz and the side of the square-shape array is $\lambda_{L1}/2$. The color indicates the AOA estimation technique evaluated: beamformer in blue, Capon in red and MUSIC in green. The marker indicates the number of interfering signals injected in the simulation: | for $\#s = 1$, \times for $\#s = 2$, Δ for $\#s = 3$ and $*$ for $\#s = 4$ (the number of straight lines required to make the symbol is equal to $\#s$).

nature of the interfering signal. Finally, for AOA estimation, the use of a higher resolution method like MUSIC achieves better results. However, it has been found that to work under suboptimal configuration arrays (i.e., with inter-element lower than half of the corresponding wavelength) reduces the number of outliers in the estimation (being avoided for the case of single interfering signals), which clearly compensates the widening effect in the corresponding beam from the spatial spectrum.

The next step will consist in building a prototype of a single GIMAD unit to tests its capabilities for interference detection, characterization, and AOA estimation in a set of field campaigns, including an initial calibration phase in an

anechoic chamber.

REFERENCES

- [1] Gromov, K., Akos, D., Pullen, S., Enge, P., and Parkinson, B., "GIDL: Generalized Interference Detection and Localization System." Proceedings of the 13th International Technical Meeting of the Satellite Division of The Institute of Navigation (ION GPS 2000), Salt Lake City, UT, September 2000, pp. 447-457.
- [2] O. Isoz, "Interference in Global Positioning System Signals and its Effect on Positioning and Remote Sensing", PhD dissertation, 2015.
- [3] B. Boashash and P. J. Black, "An efficient real-time implementation of the Wigner-Ville distribution," IEEE Trans. Acoust., Speech, Signal Process., vol. ASSP-35, no. 11, pp. 1611-1618, Nov. 1987.
- [4] R. Morales-Ferre, P. Richter, E. Falletti, A. de la Fuente and E. S. Lohan, "A Survey on Coping with Intentional Interference in Satellite Naviga-

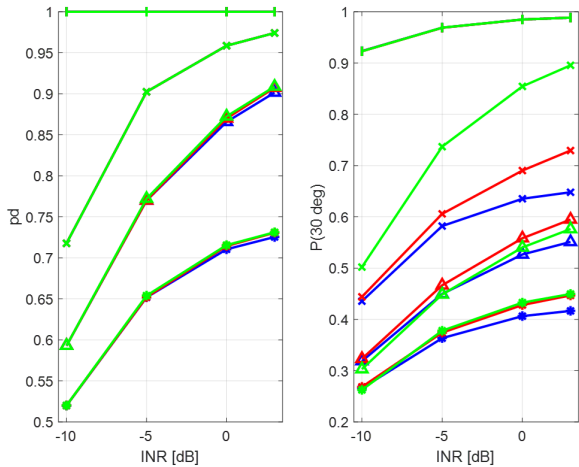


Fig. 16. [Left side] Probability of detection (AOA context) for the different techniques and number of interfering signals ($\#s$) as a function of INR. [Right side] Percentile 30° of AOA error in absolute value for the different techniques and number of interfering signals ($\#s$) as a function of INR. The frequency evaluated is 1900 MHz and the side of the square-shape array is $\lambda_{L1}/2$. The color indicates the AOA estimation technique evaluated: beamformer in blue, Capon in red and MUSIC in green. The marker indicates the number of interfering signals injected in the simulation: | for $\#s = 1$, \times for $\#s = 2$, \triangle for $\#s = 3$ and $*$ for $\#s = 4$ (the number of straight lines required to make the symbol is equal to $\#s$).

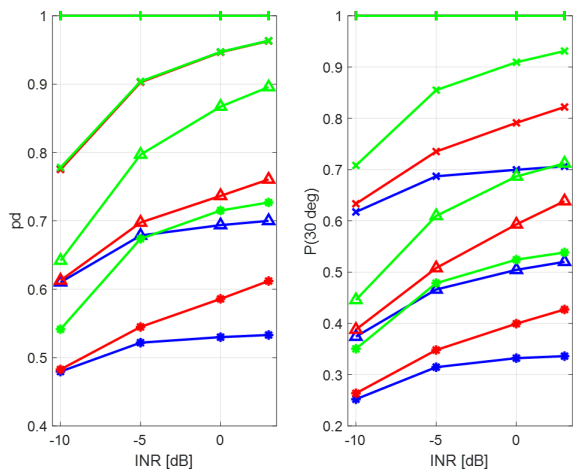


Fig. 17. [Left side] Probability of detection (AOA context) for the different techniques and number of interfering signals ($\#s$) as a function of INR. [Right side] Percentile 30° of AOA error in absolute value for the different techniques and number of interfering signals ($\#s$) as a function of INR. The frequency evaluated is GPS L1 and the side of the square-shape array is $\lambda_{L1}/3$. The color indicates the AOA estimation technique evaluated: beamformer in blue, Capon in red and MUSIC in green. The marker indicates the number of interfering signals injected in the simulation: | for $\#s = 1$, \times for $\#s = 2$, \triangle for $\#s = 3$ and $*$ for $\#s = 4$ (the number of straight lines required to make the symbol is equal to $\#s$).

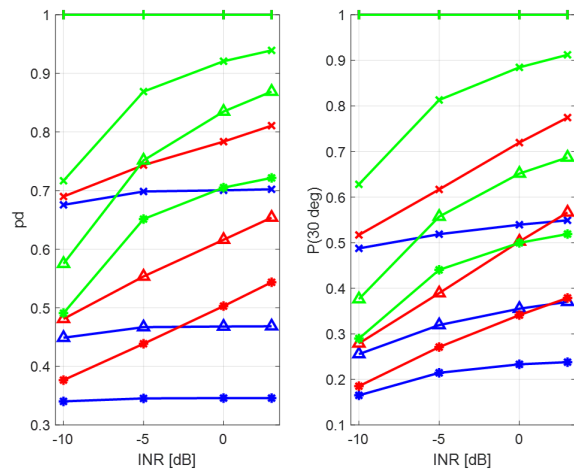


Fig. 18. [Left side] Probability of detection (AOA context) for the different techniques and number of interfering signals ($\#s$) as a function of INR. [Right side] Percentile 30° of AOA error in absolute value for the different techniques and number of interfering signals ($\#s$) as a function of INR. The frequency evaluated is GPS L5 and the side of the square-shape array is $\lambda_{L1}/3$. The color indicates the AOA estimation technique evaluated: beamformer in blue, Capon in red and MUSIC in green. The marker indicates the number of interfering signals injected in the simulation: | for $\#s = 1$, \times for $\#s = 2$, \triangle for $\#s = 3$ and $*$ for $\#s = 4$ (the number of straight lines required to make the symbol is equal to $\#s$).

tion for Manned and Unmanned Aircraft,” in *IEEE Communications Surveys & Tutorials*, vol. 22, no. 1, pp. 249-291, Firstquarter 2020.

[5] Tarongi, J.M.; Camps, A. “Normality Analysis for RFI Detection in Microwave Radiometry.” *Remote Sens.* 2010, 2, 191-210.

[6] R. D. De Roo and S. Misra, “A Moment Ratio RFI Detection Algorithm That Can Detect Pulsed Sinusoids of Any Duty Cycle,” in *IEEE Geoscience and Remote Sensing Letters*, vol. 7, no. 3, pp. 606-610, July 2010.

[7] D. Borio, L. Camoriano, S. Savasta and L. L. Presti, “Time-Frequency Excision for GNSS Applications,” in *IEEE Systems Journal*, vol. 2, no. 1, pp. 27-37, March 2008.

[8] S. Savasta, L. Lo Presti and M. Rao, “Interference Mitigation in GNSS Receivers by a Time-Frequency Approach,” in *IEEE Transactions on Aerospace and Electronic Systems*, vol. 49, no. 1, pp. 415-438, Jan. 2013.

[9] D. Borio, C. ODriscoll, and J. Fortuny, “Fast and Flexible Tracking and Mitigating a Jamming Signal With an Adaptive Notch Filter,” vol. 9, Gibbons Media, 2014.

[10] U. Bokan, M. Duregger, P. Berglez and B. Hofmann-Wellenhof, “Detection and mitigation strategies for GNSS interference Attacks”, *Vermessung & Geoinformation 2/2019*, S. 83-94.

[11] M. Sgammini, F. Antreich, and M. Meurer, “SVD-based RF interference detection and mitigation for GNSS,” in *Proc. 27th Int. Tech. Meeting Satellite Div. Inst. Navig.*, 2014.

[12] S. Bartl, P. Berglez and B. Hofmann-Wellenhof, “GNSS interference detection, classification and localization using Software-Defined Radio,” 2017 European Navigation Conference (ENC), Lausanne, 2017, pp. 159-169.

[13] M. Pini, B. Motella, and M. T. Gamba, “Detection of correlation distortions through application of statistical methods,” in *Proc. 26th Int. Tech. Meeting Satellite Div. Inst. Navig. (ION GNSS+)*, 2013.

[14] R. S. Roberts, W. A. Brown and H. H. Loomis, “Computationally efficient algorithms for cyclic spectral analysis,” in *IEEE Signal Processing Magazine*, vol. 8, no. 2, pp. 38-49, April 1991.

[15] P. Stoica and R. Moses, *Spectral analysis of signals*, Prentice-Hall, 2005.

[16] S. Weiss, M. Almah, S. Lambotharan, J. G. McWhirter and M. Kaveh, “Broadband angle of arrival estimation methods in a polynomial matrix decomposition framework,” 2013 5th IEEE International Workshop on

Computational Advances in Multi-Sensor Adaptive Processing (CAMSAP), St. Martin, 2013, pp. 109-112.

- [17] W. Coventry, C. Clemente and J. Soraghan, "Polynomial Root-MUSIC Algorithm for Efficient Broadband Direction of Arrival Estimation," 2017 Sensor Signal Processing for Defence Conference (SSPD), London, 2017, pp. 1-5.
- [18] Q. Liu, F. Yan, Y. Han, S. Liu and M. Jin, "Reduced-order root-MUSIC based on Schur spectral factorization," 2016 IEEE International Conference on Ubiquitous Wireless Broadband (ICUWB), Nanjing, 2016, pp. 1-3.
- [19] R. Roy and T. Kailath, "ESPRIT: Estimation of signal parameters via rotational invariance techniques", IEEE Trans. on Acoustics, Speech and Signal Proc., vol. 37, no. 7, pp. 984-995, July 1989.
- [20] T.K. Moon, "The expectation-maximization algorithm", IEEE Signal Processing Magazine, vol. 13, no. 6, 1996.
- [21] J.A. Fessler, A.O. Hero, "Space-alternating generalized expectation maximization algorithm", IEEE Transactions on Signal Processing, vol. 42, no. 10, October 1994.